Optimization of Magnetic Flux Ropes Modeled with the RBSL Method

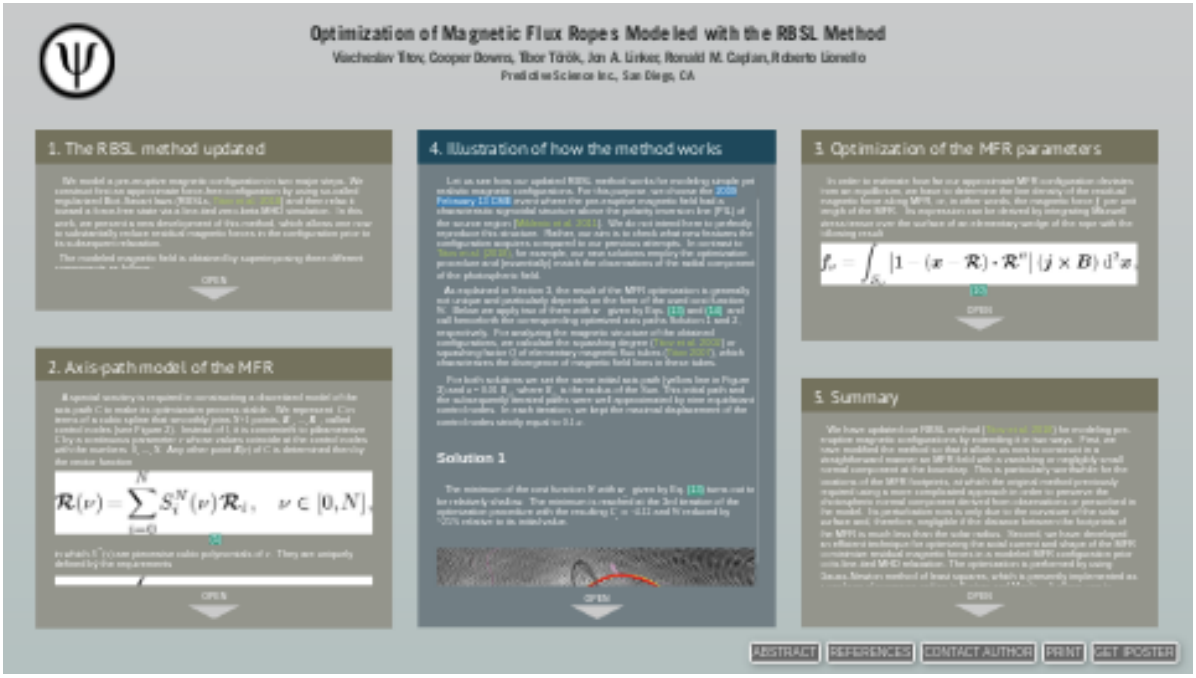

Viacheslav Titov, Cooper Downs, Tibor Török, Jon A. Linker, Ronald M. Caplan, Roberto Lionello

Predictive Science Inc., San Diego, CA

PRESENTED AT:

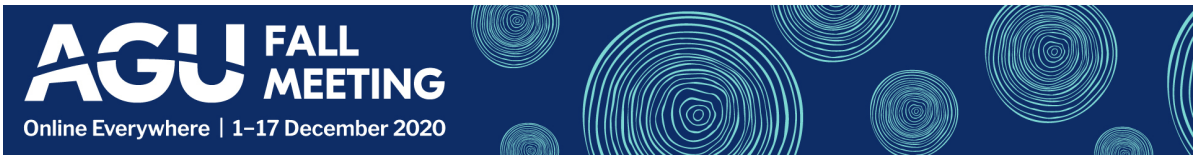

ABSTRACT

The so-called regularized Biot-Savart laws (RBSLs, Titov et al. 2018) provide an efficient and flexible method for modeling pre-eruptive magnetic configurations whose characteristics are constrained by observational image and magnetic-field data. This method allows one to calculate the field of magnetic flux ropes (MFRs) with small circular cross-sections and an arbitrary axis shape. The field of the whole configuration is constructed as a superposition of (1) such a flux-rope field, (2) an ambient potential field determined, for example, by the radial field component of an observed magnetogram, and generally (3) a so-called compensating potential field that counteracts deviations of the radial field caused by the axial current of the MFR. With an appropriate subphotospheric clousure of the MFR, we have made the compensating magnetic field negligible in the modeled configuration. The RBSL kernels are determined from the requirement that the MFR field for a straight cylinder must be exactly force-free. For a curved MFR, however, the magnetic forces are generally unbalanced over the whole path of the MFR. To reduce this imbalance, we apply a modified Gauss-Newton method to minimize the magnitude of the residual magnetic forces per unit length and the unit axial current of the MFR. This is done by iteratively adjusting the MFR axis path and axial current. We then try to relax the resulting optimized configuration in a subsequent line-tied zero-beta MHD simulation toward a force-free equilibrium. By considering several examples, we demonstrate how this approach works depending on the initial parameters of the MFR and the ambient magnetic field. Our method will be beneficial for both the modeling of particular eruptive events and theoretical studies of idealized pre-eruptive magnetic configurations.

This research is supported by NSF, NASA's DRIVE, HSR, SBIR, and LWS Programs, and AFOSR

1. THE RBSL METHOD UPDATED

We model a pre-eruptive magnetic configuration in two major steps. We construct first an approximate force-free configuration by using so-called regularized Biot-Savart laws (RBSLs, Titov et al. 2018) and then relax it toward a force-free state via a line-tied zero-beta MHD simulation. In this work, we present a new development of this method, which allows one now to substantially reduce residual magnetic forces in the configuration prior to its subsequent relaxation.

The modeled magnetic field is obtained by superimposing three different components as follows:

$$\boldsymbol{B} = \boldsymbol{B}_{\rm p} + \boldsymbol{B}_I + \boldsymbol{B}_F\,,$$

where $\boldsymbol{B}_{\rm p}$ represents the potential magnetic field produced by photospheric magnetic sources with a given distribution of the normal component of magnetic field. The other two components, $\boldsymbol{B}_I$ and $\boldsymbol{B}_F$, are, respectively, azimuthal and axial magnetic fields generated by axial net current I and axial net flux F of a thin magnetic flux rope (MFR). These components in turn are

$$\boldsymbol{B}_I = \nabla \times \boldsymbol{A}_I\,,$$
$$\boldsymbol{B}_F = \nabla \times \boldsymbol{A}_F\,,$$

where $\boldsymbol{A}_I$ and $\boldsymbol{A}_F$ are axial and azimuthal vector potentials, respectively, defined relative to the axis of MFR.

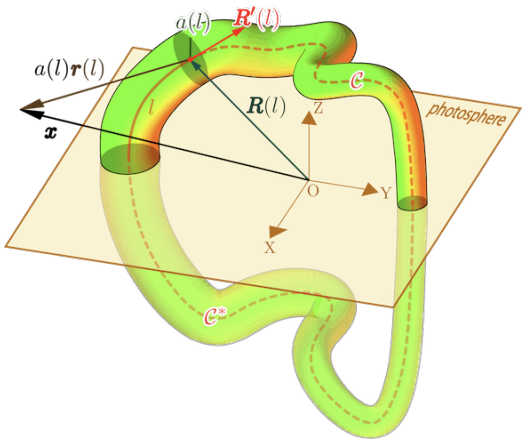

Figure 1. Magnetic flux rope (MFR) with a circular cross-section of radius $a(l)$ and coronal and subphotospheric axis paths C and C^*, respectively, defined by a radius-vector $\boldsymbol{R}(l)$, where l is the path arc length.

The axis is a closed curve consisted of coronal and subphotospheric paths, C and C^*, respectively, and represented by a vector $\boldsymbol{R}(l)$ that depends on the arc length l of the curve (Figure 1). For these vector potentials, we adopt here the RBSLs proposed earlier in (Titov et al. 2018) by assuming for simplicity that our MFR has a constant rather than variable cross-sectional radius a. Then the axial vector potential at a given point $\boldsymbol{x}$ is described by

$$\boldsymbol{A}_I(\boldsymbol{x}) = \int_{C\cup C^*} K_I(r)\,\boldsymbol{\mathcal{R}}'\,\frac{{\rm d}l}{a}\,, \qquad \left[\!\!\left[\frac{\mu I}{4\pi}\right]\!\!\right], \quad (1)$$

where $\boldsymbol{r} = \boldsymbol{r}(l) = (\boldsymbol{x} - \boldsymbol{R}(l)) / a$, $\boldsymbol{R}' = {\rm d}\boldsymbol{R}/{\rm d}l$ is a unit vector tangential to the axis path. The double brackets henceforth contain the unit in which the value displayed on the left is measured.

The RBSL-kernel of $\boldsymbol{A}_I$ is

$$K_I(r) = \begin{cases} \frac{2}{\pi}\left(\frac{\arcsin r}{r} + \frac{5-2r^2}{3}\sqrt{1-r^2}\right), & r \in (0,1], \\ r^{-1}, & r > 1, \end{cases} \quad (2)$$

whose domain of definition smoothly extends to r=0 with

$$\lim_{r\to 0^+} K_I(r) = 16/(3\pi) \approx 1.698.$$

In the limit of vanishing curvature of the MFR, this $\boldsymbol{A}_I$ by construction provides a straight cylindrical MFR with a parabolic profile of the axial current density.

We assume that the closure of the coronal current I flowing along the path C is made with a fictitious subphotospheric path C* that is simply a mirror image of C about the photospheric boundary plane. This constraint on the shape of the path allows one to *vanish* the resulting normal component of $\boldsymbol{B}_I$ at the boundary.

To cause a similar behavior of the field $\boldsymbol{B}_F$ at the boundary, we modify the azimuthal vector potential, compared to our previous approach described in (Titov et al. 2018), as

$$\begin{aligned}\boldsymbol{A}_F(\boldsymbol{x}) = &\int_{\mathcal{C}} K_F(r)\boldsymbol{\mathcal{R}}' \times \boldsymbol{r}\,\frac{\mathrm{d}l}{a} \\ &- \int_{\mathcal{C}^*} K_F(r)\boldsymbol{\mathcal{R}}' \times \boldsymbol{r}\,\frac{\mathrm{d}l}{a}, \quad \left[\!\left[\frac{F}{4\pi a}\right]\!\right].\end{aligned} \tag{3}$$

This expression implies that the corresponding axial fluxes flow along C and C* in opposite directions. Since C* is a mirror image of C about the boundary plane, these fluxes meet at the same angles to the boundary and thereby cancel each other out. Due to this trick, the resulting normal component of $\boldsymbol{B}_F$ also becomes vanishing at the boundary.

The RBSL-kernel of $\boldsymbol{A}_F$ is

$$K_F(r) = \begin{cases} \frac{2}{\pi r^2}\left(\frac{\arcsin r}{r} - \sqrt{1-r^2}\right) + \frac{2}{\pi}\sqrt{1-r^2} \\ +\frac{5-2r^2}{2\sqrt{6}}\left[1 - \frac{2}{\pi}\arcsin\left(\frac{1+2r^2}{5-2r^2}\right)\right], & r\in(0,1], \\ r^{-3}, & r>1, \end{cases} \tag{4}$$

whose domain of definition smoothly extends to r=0 with

$$\begin{aligned}\lim_{r\to 0^+} K_F(r) &= \frac{10}{3\pi} + \frac{5}{2\sqrt{6}\pi}\left[\pi - 2\arcsin\left(\frac{1}{5}\right)\right] \\ &\approx 1.951.\end{aligned}$$

In the limit of vanishing curvature of the axis path, $\boldsymbol{A}_F$ by construction provides the axial magnetic field and and azimuthal current density in a *force-free* straight cylindrical MFR with a parabolic profile of the axial current density provided

$$\frac{F}{\mu I a} \equiv \sigma = \frac{\pm 3}{5\sqrt{2}} \approx 0.424,$$

where the positive and negative signs correspond to right- and left-handed twist (chirality) of the MFR, respectively.

We assume that this relationship also holds true for a curved MFR. In this way, we manage to keep the resulting configuration as close as possible to an equilibrium for sufficiently thin MFRs, which quantitatively means that $\kappa\, a << 1$ along the axis path of curvature $\kappa(l)$. The appropriate power-law decays of $K_I(r)$ and $K_F(r)$ at r>1 ensure that, externally, our MFR manifests itself as a current and flux carrying thread described by classical Biot-Savart laws (Jackson1962).

We extend below the RBSL method by supplementing it with an optimization procedure that enables one to minimize residual magnetic forces in a modeled MFR by suitably adjusting its shape and axial current I.

2. AXIS-PATH MODEL OF THE MFR

A special scrutiny is required in constructing a discretized model of the axis path C to make its optimization process stable. We represent C in terms of a cubic spline that smoothly joins N+1 points, $\boldsymbol{R}_0$, ..., $\boldsymbol{R}_N$, called control nodes (see Figure 2). Instead of l, it is convenient to parameterize C by a continuous parameter ν whose values coincide at the control nodes with the numbers 0, ..., N. Any other point $\boldsymbol{R}(\nu)$ of C is determined then by the vector function

$$\boldsymbol{\mathcal{R}}(\nu)=\sum_{i=0}^{N} S_i^N(\nu)\,\boldsymbol{\mathcal{R}}_i\,,\quad \nu\in[0,N]\,, \tag{5}$$

in which $S_i^N(\nu)$ are piecewise cubic polynomials of ν. They are uniquely defined by the requirements

$$S_i^N(j)=\begin{cases}1 & \text{if } i=j,\quad j=0,\ldots,N,\\ 0 & \text{otherwise,}\end{cases}$$

supplemented with the corresponding smoothness and endpoint conditions at the control nodes.

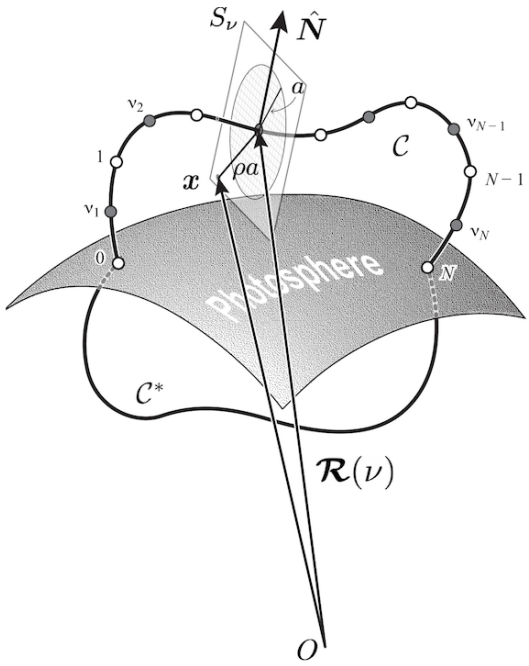

Figure 2. The coronal axis path C is represented by a vector function $\boldsymbol{R}(\nu)$, which is defined in terms of a cubic spline of N+1 equidistant control nodes $\boldsymbol{R}_i$ (white circles) uniformly parametrized by parameter ν from 0 to N. The gray circles show evaluation nodes at which the line density $\boldsymbol{f}_\nu$ of the magnetic force is calculated by Eq. (10) via the integral of the Lorentz force, taken with a certain weight, over the corresponding cross-sections S_ν perpendicular to the path. The subphotospheric axis path C^* is a copy of C mirrored about a plane that locally approximates the spherical solar boundary.

The arc length $l(\nu)$ of C as a function of ν is a solution of the following ordinary differential equation (ODE):

$$\frac{\mathrm{d}l}{\mathrm{d}\nu}=\left|\dot{\boldsymbol{\mathcal{R}}}(\nu)\right|, \tag{6}$$

in which

$$\dot{\boldsymbol{\mathcal{R}}}(\nu)=\sum_{i=0}^{N}\frac{\mathrm{d}}{\mathrm{d}\nu}S_i^N(\nu)\,\boldsymbol{\mathcal{R}}_i \quad (7)$$

is the v-derivative of Eq. (5). By integrating Eq. (6) from 0 to N, one obtains the total arc length L of C. The inverted Eq. (6) yields another ODE

$$\frac{\mathrm{d}\nu}{\mathrm{d}l}=\frac{1}{\left|\dot{\boldsymbol{\mathcal{R}}}(\nu)\right|}$$

whose solutions define the inverse relationship $v(l)$ between l- and v-parameterizations of the curve C.

The described ODEs help us to keep the control nodes $\boldsymbol{R}_i$ equidistant along the path at each iteration toward its optimized shape, which brings some kind of stiffness to the path during its deformation. The axis path defined by Eq. (5) with equidistant control nodes is henceforth called *canonical*.

The control nodes, different from the footpoints of the path, are allowed to be displaced only along the binormal $\boldsymbol{M}$ and normal $\boldsymbol{N}$ of the Frenet-Serret basis of the path. For our path model, they are calculated by using Eq. (7) and

$$\ddot{\boldsymbol{\mathcal{R}}}(\nu)=\sum_{i=0}^{N}\frac{\mathrm{d}^2}{\mathrm{d}\nu^2}S_i^N(\nu)\,\boldsymbol{\mathcal{R}}_i$$

as follows:

$$\begin{aligned}
\hat{\boldsymbol{T}}&=\boldsymbol{\mathcal{R}}'\equiv\frac{\mathrm{d}\boldsymbol{\mathcal{R}}}{\mathrm{d}l}=\frac{\dot{\boldsymbol{\mathcal{R}}}}{\left|\dot{\boldsymbol{\mathcal{R}}}\right|},\\
\hat{\boldsymbol{N}}&=\frac{\boldsymbol{\mathcal{R}}''}{\left|\boldsymbol{\mathcal{R}}''\right|},\qquad \kappa\equiv\left|\boldsymbol{\mathcal{R}}''\right|,\\
\boldsymbol{\mathcal{R}}''&\equiv\frac{\mathrm{d}^2\boldsymbol{\mathcal{R}}}{\mathrm{d}l^2}=\frac{\ddot{\boldsymbol{\mathcal{R}}}}{\dot{\boldsymbol{\mathcal{R}}}^2}-\frac{\dot{\boldsymbol{\mathcal{R}}}\cdot\ddot{\boldsymbol{\mathcal{R}}}}{\dot{\boldsymbol{\mathcal{R}}}^4}\dot{\boldsymbol{\mathcal{R}}},\\
\hat{\boldsymbol{M}}&=\hat{\boldsymbol{T}}\times\hat{\boldsymbol{N}}.
\end{aligned} \quad (8)$$

With these expressions evaluated at $v=v_j$, one can obtain the normal $\boldsymbol{N}_j$ and binormal $\boldsymbol{M}_j$ along which the corresponding control nodes $\boldsymbol{R}_j$ =1, ..., N-1, are displaced in the optimization process.

In contrast, the control nodes $\boldsymbol{R}_0$ and $\boldsymbol{R}_N$ as being the footpoints of the path are allowed to be displaced strictly along the solar surface.

This implies that

$$\begin{aligned}
\hat{\boldsymbol{M}}_0&=\hat{\boldsymbol{\theta}}_{\mathrm{FP1}},\quad \hat{\boldsymbol{M}}_N=\hat{\boldsymbol{\theta}}_{\mathrm{FP2}},\\
\hat{\boldsymbol{N}}_0&=\hat{\boldsymbol{\phi}}_{\mathrm{FP1}},\quad \hat{\boldsymbol{N}}_N=\hat{\boldsymbol{\phi}}_{\mathrm{FP2}},
\end{aligned}$$

which are the corresponding unit coordinate vectors at the footpoints of the path defined in spherical coordinate system with the origin at the center of the Sun. Thus, a small variation of the axis path described by Eq. (5) can be written as

$$\delta\boldsymbol{\mathcal{R}}=a\sum_{i=0}^{N}S_i^N(\nu)\left(\xi_i\hat{\boldsymbol{M}}_i+\eta_i\hat{\boldsymbol{N}}_i\right), \quad (9)$$

where the node displacements ξ_i and η_i are normalized to a. We hold these displacements to be << 1 through all iterations of the

optimization process.

The subphotospheric axis path C^* at each iteration is chosen to be a copy of C mirrored about the plane that passes through the footpoints $\boldsymbol{R}_0$ and $\boldsymbol{R}_N$ and has the normal

$$\hat{\boldsymbol{n}} = \boldsymbol{\mathcal{O}}/|\boldsymbol{\mathcal{O}}|\,,$$

where

$$\boldsymbol{\mathcal{O}} = (\boldsymbol{\mathcal{R}}_0 + \boldsymbol{\mathcal{R}}_N)/2$$

is an average of the footpoints. For the distance between $\boldsymbol{R}_0$ and $\boldsymbol{R}_N$ much smaller than the radius of the Sun, this plane well approximates a plane touching the solar surface at the point $\boldsymbol{O}$. The corresponding mirror images of the control nodes are given by

$$\boldsymbol{\mathcal{R}}_i^* = \boldsymbol{\mathcal{R}}_i - 2\hat{\boldsymbol{n}}\cdot(\boldsymbol{\mathcal{R}}_i - \boldsymbol{\mathcal{O}})\hat{\boldsymbol{n}}\,.$$

By using the same direction and type of parameterization as for the path C (Eq. (5)), one can determine its corresponding mirrored points at C^* from

$$\boldsymbol{\mathcal{R}}^*(\nu) = \sum_{i=N}^{0} S_i^N(\nu)\,\boldsymbol{\mathcal{R}}_i^*\,, \quad \nu \in [0,N]\,.$$

This closure of C makes it possible to minimize the normal component of magnetic field that the flux-rope currents produce at the boundary, as mentioned above. The normal component of the resulting field then is almost due to the potential field $\boldsymbol{B}_{\rm p}$, or, in other words, it becomes almost identical to the component derived from observations. A difference between them is only due to the curvature of the solar surface, which is relatively small for typical source regions of CMEs. The configurations of a larger size require a more sophisticated approach, which will be published separately elsewhere.

3. OPTIMIZATION OF THE MFR PARAMETERS

In order to estimate how far our approximate MFR configuration deviates from an equilibrium, we have to determine the line density of the residual magnetic force along MFR, or, in other words, the magnetic force $\boldsymbol{f}_\nu$ per unit length of the MFR. Its expression can be derived by integrating Maxwell stress tensor over the surface of an elementary wedge of the rope with the following result

$$\boldsymbol{f}_\nu = \int_{S_\nu} \left|1 - (\boldsymbol{x} - \boldsymbol{\mathcal{R}}) \cdot \boldsymbol{\mathcal{R}}''\right| (\boldsymbol{j} \times \boldsymbol{B})\, \mathrm{d}^2\boldsymbol{x}\,, \quad (10)$$

where $\boldsymbol{R}$ and $\boldsymbol{R}$" are given for our path model by Eqs. (5) and (8). One can show that $\boldsymbol{f}_\nu$ is very sensitive to the curvature of the path, which motivated us to evaluate it for the purpose of optimization at points different from the control nodes $\boldsymbol{R}_i$, because it tends to have local maxima at $\boldsymbol{R}_i$. For the evaluation of $\boldsymbol{f}_\nu$, therefore, we choose the points that are equidistantly separated from the nearest control nodes.

The total current density in our RBSL flux rope is

$$\boldsymbol{j} = \boldsymbol{j}_I + \sigma \boldsymbol{j}_F\,, \qquad \left[\!\!\left[\frac{I}{4\pi a^2} \right]\!\!\right],$$

where $\boldsymbol{j}_I$ and $\boldsymbol{j}_F$ are axial and azimuthal current densities, whose expressions can be derived from Eqs. (1)-(2) and (3)-(4), respectively.

Let the potential field $\boldsymbol{B}_\mathrm{p}$ and axial current I be measured in B_u and I_u units, respectively, such that

$$I_\mathrm{u} = 4\pi a B_\mathrm{u}/\mu$$

and so

$$I = C_I I_\mathrm{u}\,,$$

where the dimensionless coefficient C_I is yet to be determined in further optimization. Then $\boldsymbol{f}_\nu$ can be written as

$$\boldsymbol{f}_\nu = C_I \boldsymbol{f}_{\nu_\mathrm{p}} + C_I^2 \boldsymbol{f}_{\nu_{IF}}\,, \qquad \left[\!\!\left[\frac{B_\mathrm{u}^2}{\mu} a \right]\!\!\right], \quad (11)$$

where the first and second terms are two separate parts of $\boldsymbol{f}_\nu$ due to $\boldsymbol{j} \times \boldsymbol{B}_\mathrm{p}$ and $\boldsymbol{j} \times (\boldsymbol{B}_I + \sigma\, \boldsymbol{B}_F)$, respectively. The current density and magnetic field components are calculated here by using differential formulations of RBSLs, which allow one to represent our RBSL integrals as solutions of certain ODEs. This makes it possible to exploit the power of the adaptive step refinement in the existing ODE solvers for calculating the required integral values.

On the basis of the derived $\boldsymbol{f}_\nu$, we constructed several metrics for measuring how far from equilibrium an MFR configuration is and used them as cost functions in a minimization procedure to obtain approximate equilibria. The construction invokes the nonlinear least squares method and the corresponding minimization is performed iteratively by varying MFR parameters, namely, the axial current and coordinates of the control nodes. More precisely, these parameters include the dimensionless parameter C_I and $2(N+1)$-dimensional vector of the node displacements

$$\boldsymbol{\chi} = (\xi_0, \ldots, \xi_N, \eta_0, \ldots, \eta_N)^\mathrm{T}\,,$$

where the subscript T denotes matrix transposition. The metrics or cost functions are constructed as a mean square of a 3D vector characteristic $\boldsymbol{w}_\nu$ of magnetic forces determined at cross-sections S_ν, which in matrix notations is

$$W = \frac{1}{N} \sum_{\nu=\nu_1}^{\nu_N} \boldsymbol{w}_\nu^\mathrm{T} \boldsymbol{w}_\nu\,. \quad (12)$$

We have found that two of such characteristics provide the most interesting results.

The first characteristics is derived from Eq. (10) by dividing it on I.

After normalizing it in the same way as Eq. (11), one obtains

$$\boldsymbol{w}_\nu = \boldsymbol{f}_{\nu_\mathrm{p}} + C_I \boldsymbol{f}_{\nu\,IF}\,, \qquad \left[\!\!\left[\frac{B_\mathrm{u}}{4\pi} \right]\!\!\right], \quad (13)$$

which is nothing else than a residual magnetic force per unit current and per unit length of the MFR. Thus, the cost function based on this characteristic is simply a mean square of the effective magnetic field with which the currents of the rope interact.

The second characteristic is derived by dividing Eq. (13) on the normalized self-force $C_I\,|\boldsymbol{f}_{\nu\,IF}|$, which yields

$$\boldsymbol{w}_\nu = \frac{C_I^{-1}\boldsymbol{f}_{\nu_\mathrm{p}} + \boldsymbol{f}_{\nu\,IF}}{|\boldsymbol{f}_{\nu\,IF}|}\,. \quad (14)$$

Although both introduced cost functions reach the same absolute minimum $W = 0$ at vanishing $|\boldsymbol{f}_\nu|$, their minimization yields generally different results with different nonvanishig minimums of W. Note that the parameter C_I ($1/C_I$) enters quadratically into the first (second) W, which allows one to find immediately its optimal value for a given axis path. In the first case, we obtain

$$C_I = -\sum_{\nu=\nu_1}^{\nu_N} \boldsymbol{f}_{\nu_\mathrm{p}}^\mathrm{T}\boldsymbol{f}_{\nu\,IF} \Bigg/ \sum_{\nu=\nu_1}^{\nu_N} |\boldsymbol{f}_{\nu\,IF}|^2 \quad (15)$$

and in the second case

$$C_I = -\sum_{\nu=\nu_1}^{\nu_N} \frac{|\boldsymbol{f}_{\nu_\mathrm{p}}|^2}{|\boldsymbol{f}_{\nu\,IF}|^2} \Bigg/ \sum_{\nu=\nu_1}^{\nu_N} \frac{\boldsymbol{f}_{\nu_\mathrm{p}}^\mathrm{T}\boldsymbol{f}_{\nu\,IF}}{|\boldsymbol{f}_{\nu\,IF}|^2}\,. \quad (16)$$

The optimization of the axis path is a less trivial problem that generally can be tackled only numerically, because both cost functions have a very complex nonlinear dependence on coordinates of the control nodes. Therefore, we will solve this numerical problem iteratively in small steps. Let us first perturb $\boldsymbol{w}_\nu$ with small displacements of the nodes (Eq. (9)) and linearize it around an unperturbed path to obtain

$$\boldsymbol{w}_\nu \approx \boldsymbol{w}_\nu^0 + \mathbf{J}_\nu\boldsymbol{\chi}, \quad (17)$$

where $\boldsymbol{w}_\nu^0$ is the unperturbed characteristic and

$$(\mathbf{J}_\nu)_{ij} \equiv \frac{\partial w_\nu^i}{\partial \chi^j}$$

is a $3 \times 2(N+1)$-dimensional Jacobian matrix determined numerically in terms of Fréchet derivatives along the basis vectors $\boldsymbol{M}_j$ and $\boldsymbol{N}_j$, $j = 0, ..., N$. The substitution of Eq. (17) into Eq. (12) turns W into a quadratic form in $\boldsymbol{\chi}$ with a symmetric and positive definite matrix $\mathbf{J}^\mathrm{T}_\nu\,\mathbf{J}_\nu$, so that with the minimization of this form we arrive at the classical Gauss–Newton method (Fletcher 2000). This method alone, however, is not sufficient for our purposes, as it may generally result in $|\boldsymbol{\chi}|$ that is too large in value and, therefore, invalidate our linearization approach.

To be self-consistent with this approach, one needs to minimize W subject to the constraint $\boldsymbol{\chi}^\mathrm{T}\boldsymbol{\chi} = \mathrm{const} \ll 1$. This is reached by extending the cost function as follows:

$$W = \frac{1}{N}\sum_{\nu=\nu_1}^{\nu_N} \boldsymbol{w}_\nu^\mathrm{T}\boldsymbol{w}_\nu + \lambda\boldsymbol{\chi}^\mathrm{T}\boldsymbol{\chi},$$

where λ is a Lagrange multiplier, known in the least-squares method as damping parameter (Levenberg 1944; Marquardt 1963). Taking the derivative of this extended cost function with respect to $\boldsymbol{\chi}$ and setting the result to zero yields the following linear system of so-called normal equations:

$$\left(\sum_{\nu=\nu_1}^{\nu_N} \mathbf{J}_\nu^{\mathrm{T}} \mathbf{J}_\nu + \lambda \mathbf{I} \right) \boldsymbol{\chi} = - \sum_{\nu=\nu_1}^{\nu_N} \mathbf{J}_\nu^{\mathrm{T}} \boldsymbol{w}_\nu^0 \,. \quad (18)$$

In this form, the derived system is applicable to both cases defined by Eqs. (13) and (14). However, their Jacobian matrices are different: in the first case

$$\mathbf{J}_\nu = \mathbf{J}_{\nu_{\mathrm{p}}} + C_I \mathbf{J}_{\nu_{IF}}$$

where

$$\left(\mathbf{J}_{\nu_{\mathrm{p}}}\right)_{ij} \equiv \frac{\partial f^i_{\nu_{\mathrm{p}}}}{\partial \chi^j} \,,$$
$$\left(\mathbf{J}_{\nu_{IF}}\right)_{ij} \equiv \frac{\partial f^i_{\nu_{IF}}}{\partial \chi^j} \,,$$

and in the second case

$$\mathbf{J}_\nu = \frac{1}{|\boldsymbol{f}_{\nu_{IF}}|} \left(C_I^{-1} \mathbf{J}_{\nu_{\mathrm{p}}} + \mathbf{J}_{\nu_{IF}} - \frac{\boldsymbol{w}_\nu^0}{|\boldsymbol{f}_{\nu_{IF}}|} \boldsymbol{f}_{\nu_{IF}}^{\mathrm{T}} \mathbf{J}_{\nu_{IF}} \right) .$$

To initialize optimization procedure, we first reconstruct an approximate axis path of the MFR by using observational data and convert it to the canonical form, as described in Section 2. For this canonical path, we compute then the corresponding $\boldsymbol{w}_\nu$ and $\mathbf{J}_\nu$. By putting $\boldsymbol{w}_\nu^0 = \boldsymbol{w}_\nu$ in Eq. (18) we solve it for $\boldsymbol{\chi}$ at several different values of the parameter $\lambda > 0$ until the inequality $\max |\boldsymbol{\chi}| \ll 1$ is satisfied. We consider that $\boldsymbol{\chi}$ satisfying this inequality is an acceptable solution, which we use then to calculate by Eqs. (5) and (9) a new axis path $\boldsymbol{R} + \delta\boldsymbol{R}$ for the next iterate. We iterate in this manner until W stops decreasing. The canonical path in this sequence of iterates that corresponds to a minimum of W is regarded as a sought-for optimal path.

From the standpoint of the minimization of W only, it would be self-consistent to use at each iterate the expression for C_I derived from the same W as the normal equations. However, if one takes into account the subsequent MHD relaxation of the resulting optimized configuration, this part of the method has to be modified.

It turns out that, for configurations with the ambient potential field of a bipolar type, Eq. (15) provides C_I of somewhat low values, such that the corresponding MFRs after relaxation appear to be pushed too much downward to the solar surface and, therefore, to be partially deprived of the initial coherency in the structure. In this respect, the use of Eq. (16) for C_I leads to better equilibria, where the MFRs hover over the surface or barely touch it as well-defined entities. Bearing this in mind, we have employed only Eq. (16) irrespective of which cost function W is used for optimizing axis paths.

4. ILLUSTRATION OF HOW THE METHOD WORKS

Let us see how our updated RBSL method works for modeling simple yet realistic magnetic configurations. For this purpose, we choose the 2009 February 13 CME event where the pre-eruptive magnetic field had a characteristic sigmoidal structure above the polarity inversion line (PIL) of the source region (Miklenic et al. 2011). We do not intend here to perfectly reproduce this structure. Rather, our aim is to check what new features the configuration acquires compared to our previous attempts. In contrast to Titov et al. (2018), for example, our new solutions employ the optimization procedure and (essentially) match the observations of the radial component of the photospheric field.

As explained in Section 3, the result of the MFR optimization is generally not unique and particularly depends on the form of the used cost function W. Below we apply two of them with $\boldsymbol{w}_v$ given by Eqs. (13) and (14) and call henceforth the corresponding optimized axis paths Solution 1 and 2, respectively. For analyzing the magnetic structure of the obtained configurations, we calculate the squashing degree (Titov et al. 2002) or squashing factor Q of elementary magnetic flux tubes (Titov 2007), which characterizes the divergence of magnetic field lines in these tubes.

For both solutions we set the same initial axis path (yellow line in Figure 3) and $a = 0.01\ R_\odot$, where $R_\odot$ is the radius of the Sun. This initial path and the subsequently iterated paths were well approximated by nine equidistant control nodes. In each iteration, we kept the maximal displacement of the control nodes strictly equal to $0.1\ a$.

Solution 1

The minimum of the cost function W with $\boldsymbol{w}_v$ given by Eq. (13) turns out to be relatively shallow. The minimum is reached at the 3rd iteration of the optimization procedure with the resulting $C_I \simeq -4.12$ and W reduced by ~25% relative to its initial value.

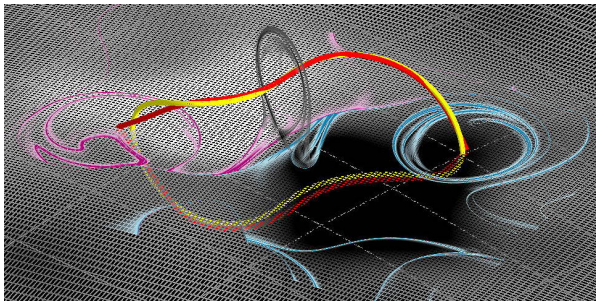

Figure 3. The initial (yellow) vs. optimized (red) axis path of Solution 1; the photospheric B_r-map (grayshaded) is shown with the used grid oulined in gray; for the optimized configuration, and B_r-signed $\log_{10}(Q)$ map (sky-blue for negative and crimson for positive polarities, respectively; the saturation level for the distirubiton is $\log_{10}(Q)$=4.0) is superimposed on top of the B_r-map; the middle cross-section displays the corresponding $\log_{10}(Q)$-distribution by using the inverted grayscale palette with fully transparent colors at $\log_{10}(Q)$<2. The same color coding is used for similar maps below.

The magnetic topology of the optimized configuration prior to MHD relaxation

The structural skeleton of the optimized configuration is formed by two bald-patch separatrix surfaces (BPSSs) originating at two segments of the polarity inversion line (PIL) of the photospheric B_r-distribution. These BPSSs divide the volume enclosing the MFR into several domains and contain so-called BP-BP separators (**red**, **orange**, and **magenta** thick lines in Figure 4), which are the field lines that touch the photosphere at two different bald-patch (BP) points of the PIL and lie at the intersection of two BPSSs (Titov & Démoulin 1999).

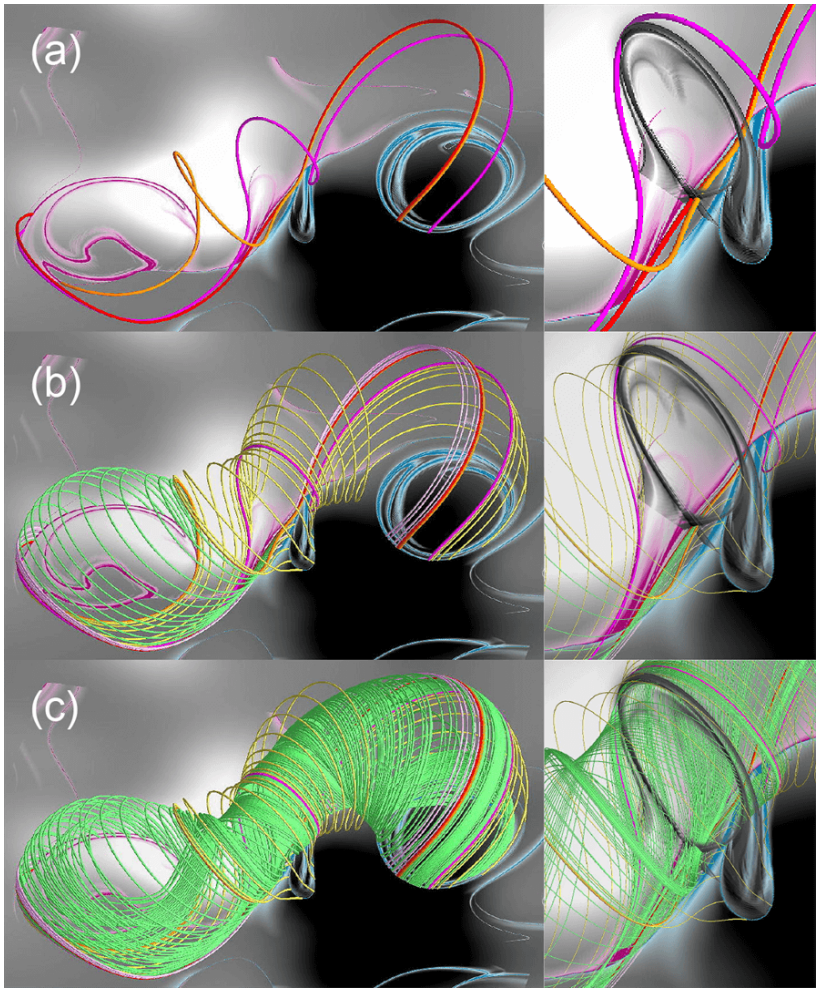

Figure 4. BPSS structure of the optimized MFR configuration: (a) BP-BP separators (**red**, **orange**, and **magenta**), (b) BPSS (yellow field lines) that envelopes the MFR, BPSSs (light-magenta field lines) that bounds a small arcade below the MFR, and BPSS (green field lines) that fills a gap between two separators (red and orange thick lines) and belongs to the MFR boundary, (c) BPSS (green field lines) that bounds the MFR itself; additional panels in the right column show zoomed regions in the middle of the structure to reveal the relations between the field lines and the corresponding cross-sectional $\log_{10}(Q)$-map.

The separator colored in **red** in Figure 4 lies at the intersection of two BPSSs below the MFR and is very similar to the one discovered earlier by Titov & Démoulin (1999) in a simple analytical model of a pre-eruptive configuration with a toroidal-arc MFR. In addition, the structural skeleton of Solution 1 has several other topological features, which are not covered by that model. The most interesting of them is the BPSS that envelopes and touches the MFR boundary along the other separator (thick **magenta** line in Figure 4). The appearance of this feature is likely due to the fact that, by construction, the used superposition of the MFR and ambient potential fields does not perturb the prescribed photospheric B_r-distribution.

Although all these BPSSs disappear in subsequent line-tied MHD relaxation, the resulting relaxed configuration acquires several quasi-separatrix layers (QSLs, Priest & Démoulin 1995; they are identified here through the squashing factor Q as defined by Titov 2007), which provide a similar partition of the core field of the configuration (see Figures 5-7).

The optimized configuration before and after line-tied MHD relaxation

Due to relatively large unbalanced residual forces, the optimized configuration undergoes a dramatic transformation during the line-tied relaxation toward a force-free state (cf. panels (a) and (b) in Figure 5). By comparing congutate footpoins of the field lines before and after the relaxation (cf. panels (c) and (d) in Figure 5), one can see that this transformation is realized by magnetic reconnection with a significant change of the field-line connectivity. It is of particular interest that the relaxation results in a qualitatively different distribution of the electric current (cf. panels (e) and (f) in Figure 5).

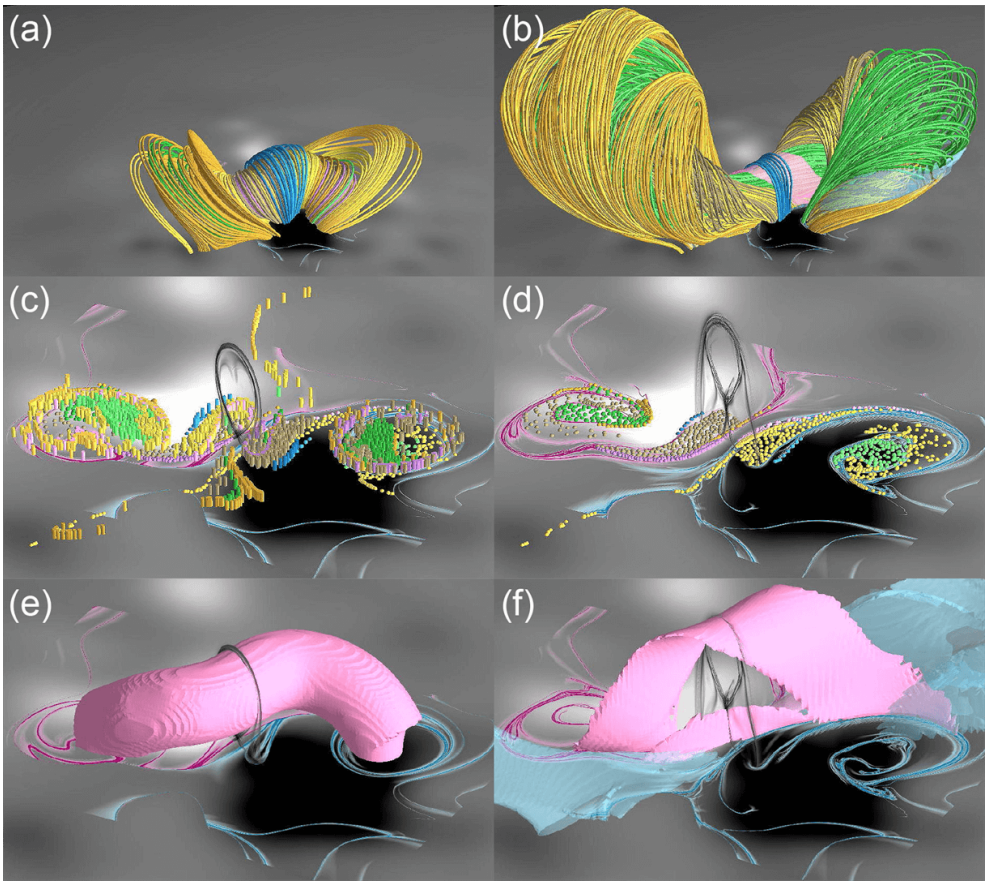

Figure 5. The elements of the configuration before (left column) and after (right column) line-tied zero-beta MHD relaxation. The field lines shown in panels (a) and (b) have the same footpoints; the latter are depicted in panels (c) and (d) by small balls, which together with small bars of the same color in panel (c) represent the conjugate footpoints. Panels (e) and (f) show the corresponding iso-surfaces $j/j_{max} = 0.438$ (magenta) of the current density. Panel (f) also presents an iso-surface $\alpha/|\alpha|_{max} = 0.079$ (semi-transparent cyan) of the force-free parameter to designate a layer of return current.

The outermost set of field lines (blue) in the middle of the structure is a magnetic arcade that envelopes the core of the relaxed configuration, which contains a sigmodial MFR (green) encompassing almost untwisted flux and two magnetic loops (yellow; called below "arms") adjacent to the lateral sides of the MFR. In the middle of the configuration, these loops are nearly horizontal and adjoined to a vertical current layer. The loops are larger in size than the envelope arcade and, at larger distances from the current layer, wrap around the MFR (see Figure 5b and 6) to add twist and sigmoidality to the core structure.

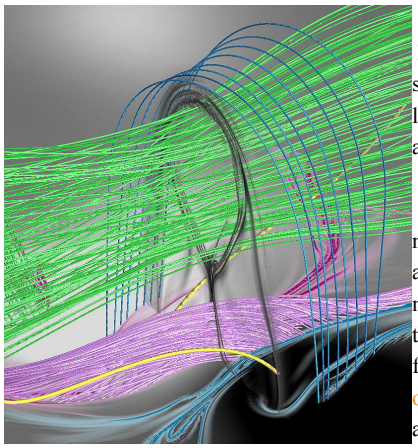

Figure 6. A zoomed region of the relaxed configuration near its middle cross-section: the field lines of the envelope arcade (blue), MFR (green), vertical current layer (light-magenta), and flux tubes (yellow thick lines; called "arms" below) adjacent to the current layer are shown.

The vertical current layer has three sublayers with the central sublayer being a narrow sheared arcade of relatively short field lines (light-magenta in Figure 6) that are aligned along the PIL. The adjacent other two sublayers (see Figure 7f) contain much longer field lines arching above the MFR and current layer, so that one of their footpoints resides next to the sheared arcade, while the other lies far away from the PIL on the outskirt of the conjugate polarity. These field lines, colored in orange in Figure 5b, have similar shapes as the neighboring yellow ones, but they are interlocked with the MFR field lines (green) differently. Features such as the vertical current layer with the neighboring sheared field lines are generic for many existing models of pre-eruptive configurations (e.g., see Kusano et al. 2012 and Xia et al. 2014).

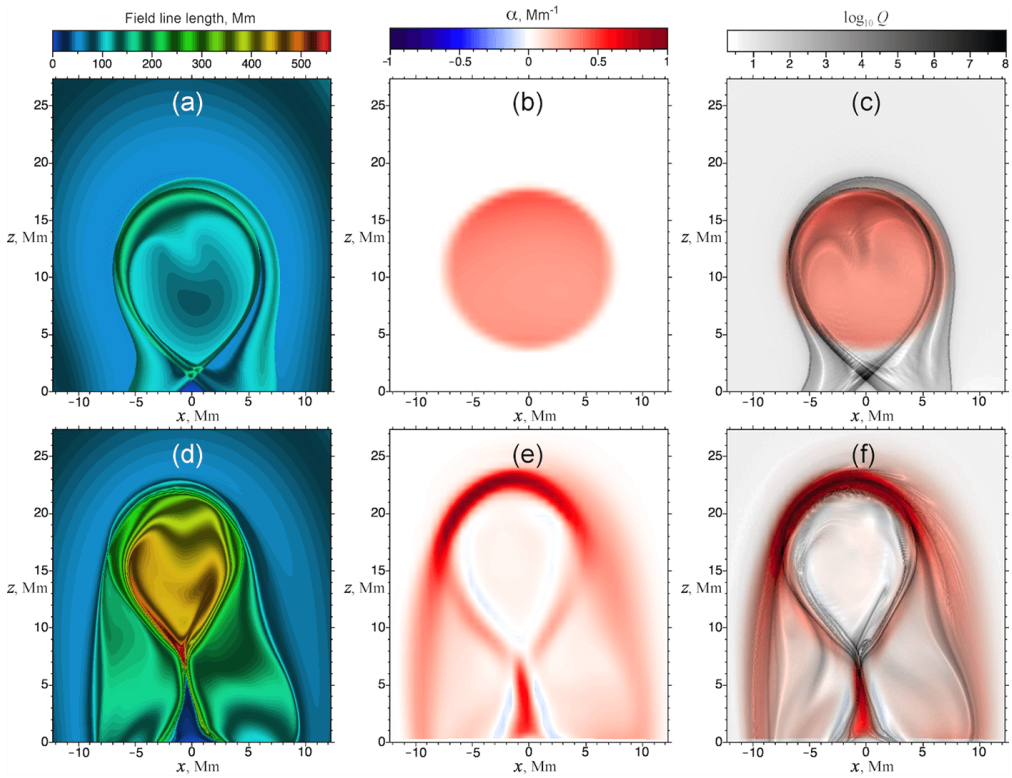

Figure 7. Maps of the field line length (1st column), force-free parameter α (2nd column), and $\log_{10}(Q)$ (3rd column) in the middle cross-section for Solution1 before (1st row) and after (2nd row) line-tied zero-beta MHD relaxation of the optimized configuration. The greyshaded $\log_{10}(Q)$–maps are blended with the corresponding blue-red α-maps.

It is very instructive to compare maps of the force-free parameter α and $\log_{10}(Q)$ in the middle cross-section of the optimized configuration before and after its relaxation (Figure 7). This comparison shows that the axial current distributed initially across the MFR transforms during the relaxation into several force-free current layers aligned with the QSLs in the configuration.

Solution 2

The minimum of the cost function W with $\boldsymbol{w}_v$ given by Eq. (14) is also relatively shallow. It is reached at the 4th iteratation of the optimization procedure with the resulting $C_J \simeq$ -3.72 and W reduced by ~24% relative to its initial value.

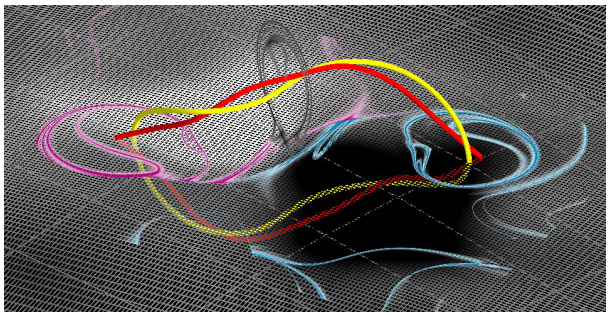

Figure 8. The initial (yellow) vs. optimized (red) axis path of Solution 2; photospheric B_r-map (grayshaded) is shown with the used grid oulined in gray; for the optimized configuration, and B_r-signed $\log_{10}(Q)$ map (sky-blue for negative and crimson for positive polarities, respectively; the saturation level for the distirubiton is $\log_{10}(Q)$=4.0) is superimposed on top of the B_r-map; the middle cross-section displays the corresponding $\log_{10}(Q)$-distribution by using the inverted grayscale palette with fully transparent colors at $\log_{10}(Q)$<2. The same color coding is used for similar maps below.

Due to a lower value of the resulting optimized axial current, the relaxed configuration has a more compact structure compared to Solution 1. In contrast to the latter, the middle part of the MFR is pushed during the relaxation downward to the boundary, which prevents the formation of a vertical current layer. In all other respects, Solution 1 and 2 are very similar (see Figures 9-11).

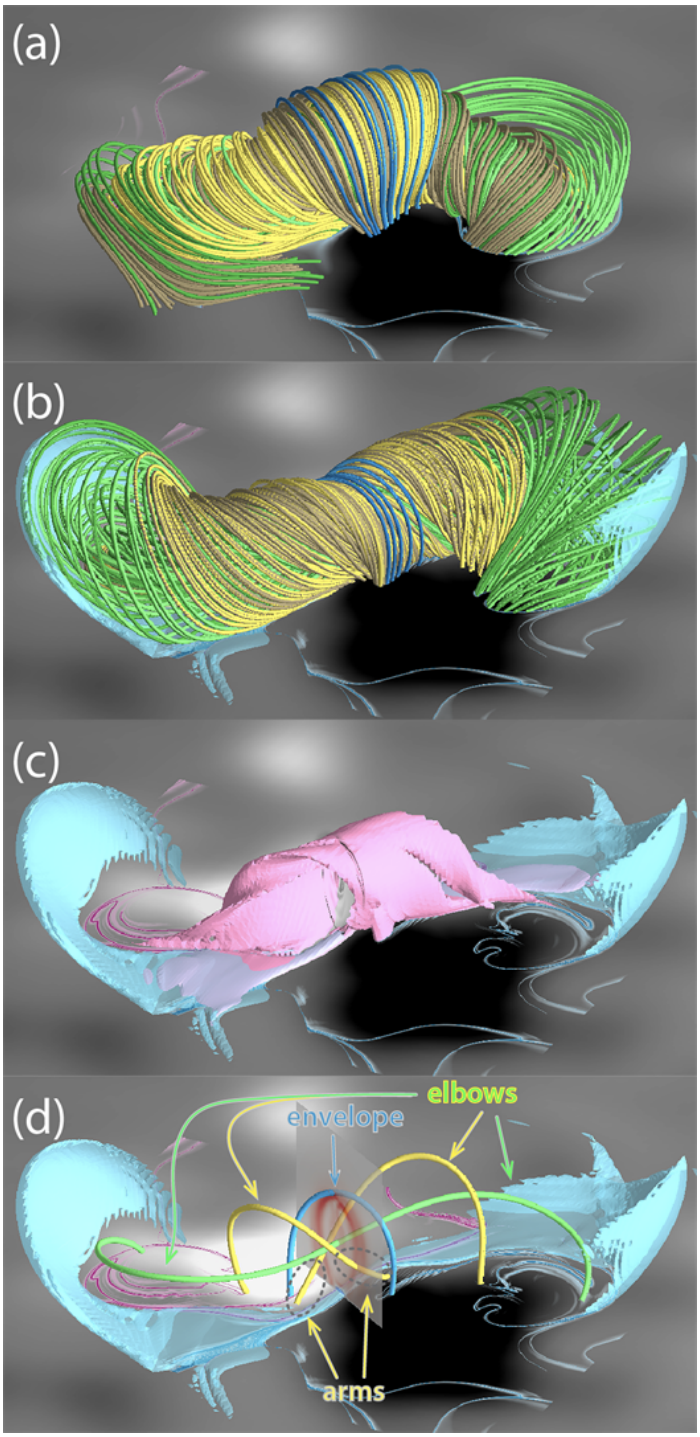

Figure 9. The magnetic structure of the MFR configuration described by Solution 2: the optimized configuration before (a) and after (b,c,d) line-tied zero-beta MHD relaxation with three major types of field lines (d) that form the resulting configuration; (c) the corresponding iso-surfaces of the current density $j/j_{max} = 0.438$ (magenta) and force-free parameter $\alpha/|\alpha|_{max} = 0.079$ (semi-transparent cyan); the field lines shown in panels (a) and (b) have the same footpoints. Panel (d) presents also the corresponding α-map in the middle cross-section of the configuration and several representative field lines that succinctly illustrate the structure.

Figure 10 shows maps of the force-free parameter α and $\log_{10}(Q)$ in the middle cross-section of the optimized configuration before and after line-tied MHD relaxation. As for Solution 1, it demonstrates that the current density distributed initially over the entire cross-section of the MFR transforms during the relaxation into several current layers aligned with the QSLs that are formed in the configuration by this process.

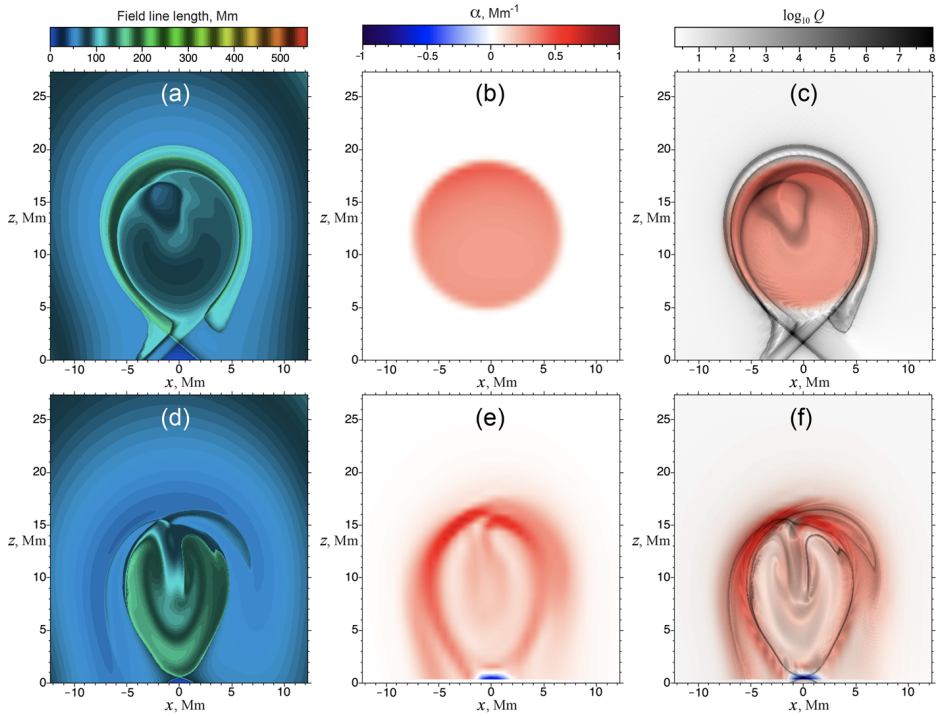

Figure 10. Maps of the field line length (1st column), force-free parameter α (2nd column), and $\log_{10}(Q)$ (3rd column) in the middle cross-section for Solution1 before (1st row) and after (2nd row) line-tied zero-beta MHD relaxation of the optimized configuration. The greyshaded $\log_{10}(Q)$–maps are blended with the corresponding blue-red α-maps.

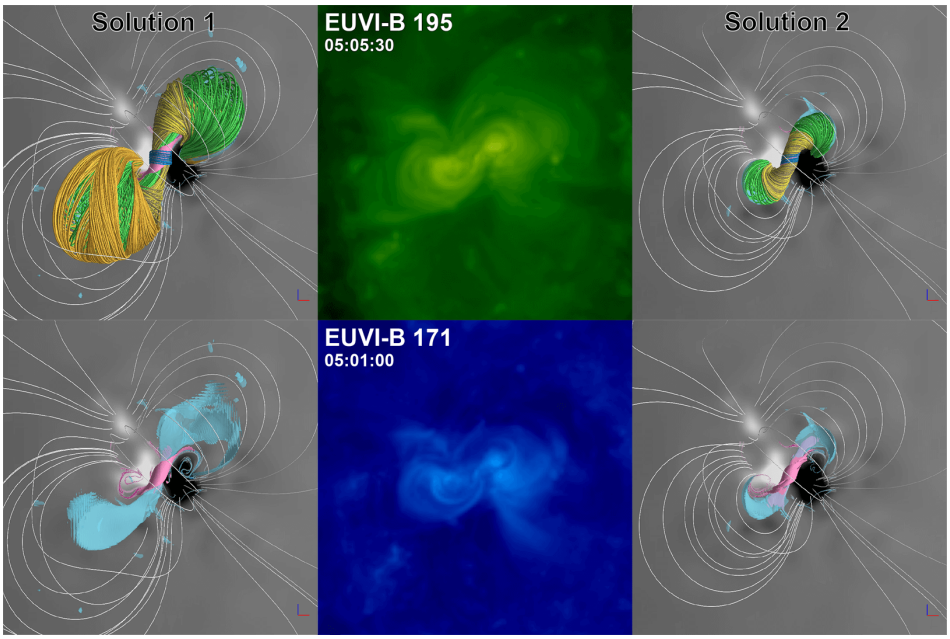

Figure 11. Top view of the field-line structure (1st raw) and j/j_{max} = 0.438 (magenta) and $\alpha/|\alpha|_{max}$ = 0.079 (semi-transparent cyan) isosurfaces (2nd raw) corresponding to our solutions vs. EUV images (2nd column) of the pre-eruptive configuration of the 2009 February 13 CME event.

Figure 11 enables us to compare the obtained solutions with the corresponding EUV images of the pre-eruptive configuration. One can see that both solutions satisfactorily reproduce the observed sigmoidal shape of the core field. However, the size of the

sigmoid of Solution 2 apparently corresponds much better to the observations. This comparison shows that the result of the relaxation is rather sensitive to the choice of the cost function in the optimization procedure.

It is interesting that our previous model (Titov et al. 2018) did not invoke the optimization of the MFR parameters and did not preserve the radial component of the photospheric field obtained from observations at the footprints of the MFR. Nevertheless, it also qualitatively reproduced the sigmoid shape starting from a different initial axis path with the footpoints anchored to the photosphere. This indicates a certain robustness of the RBSL method used in both models.

In conclusion, it should be emphasized that our particular Solutions 1 and 2 qualitatively describe also the magnetic structure of other sigmoidal pre-eruptive configurations. Indeed, the representative field lines shown in Figure 9d can easily be identified as "envelope", "elbows", and "arms" revealed in different observations of typical eruptive events occuring in bipolar active regions (Moore et al. 2001).

5. SUMMARY

We have updated our RBSL method (Titov et al. 2018) for modeling pre-eruptive magnetic configurations by extending it in two ways. First, we have modified the method so that it allows us now to construct in a straightforward manner an MFR field with a vanishing or negligibly small normal component at the boundary. This is particularly worthwhile for the locations of the MFR footprints, at which the original method previously required using a more complicated approach in order to preserve the photospheric normal component derived from observations or prescribed in the model. Its perturbation now is only due to the curvature of the solar surface and, therefore, negligible if the distance between the footprints of the MFR is much less than the solar radius. Second, we have developed an efficient technique for optimizing the axial current and shape of the MFR to minimize residual magnetic forces in a modeled MFR configuration prior to its line-tied MHD relaxation. The optimization is performed by using Gauss-Newton method of least squares, which is presently implemented as a package of programs written in Fortran and Maple. It allows one to make the optimization on laptops within less than hour for the cases considered so far. The performance can be improved by implementing the optimization method fully in Fortran.

We have applied our updated method to modeling pre-eruptive configurations of the February 13 CME event. This application has demostrated the viability of the method and revealed its new capabilities. Our optimized solutions were relaxed in line-tied zero-beta MHD simulations toward force-free states to provide sigmodial configurations whose cores have a nontrivial magnetic structure. The cores contain an MFR nested within a sheared magnetic arcade, which are both separated from the neighboring structure by curved current layers. Depending on how large the total axial current in the relaxed configuration is, the core can also contain a vertical current layer nested below the MFR within the arcade. This vertical current layer itself is another sheared arcade of a smaller height whose central narrow region is filled with short field lines. It is interesting that all these current layers are well aligned with QSLs formed in the configuration during its relaxation. The partition of the core field by the QSLs reveals building blocks that match very well to morphological features typically observed in eruptive configurations with a bipolar distribution of the photospheric magnetic field (Moore et al. 2001).

The demonstrated new capabilities of the updated RBSL method suggest that it will be beneficial for the modeling of particular eruptive events as well as for theoretical studies of idealized pre-eruptive magnetic configurations.

Acknowledgement

This research is supported by NSF, NASA's DRIVE, HSR, SBIR, and LWS Programs, and AFOSR.

REFERENCES

Fletcher, R. 2000, Practical Methods of Optimization, 2nd edn (Wiley, 436 p.)

Jackson, J. D. 1962, Classical Electrodynamics (New York: Wiley, 808 p.)

Kusano, K., Bamba, Y., Yamamoto, T. T., et al. 2012, ApJ, **760**, 31

Levenberg, K. 1944, Quart. Appl. Math., **2**, 164

Marquardt, D. W. 1963, J. Soc. for Indust. and Appl. Math., **11**, 431

Miklenic, C., Veronig, A. M., Temmer, M., Möstl, C., & Biernat, H. K. 2011, SoPh, **273**, 125

Moore, R. L., Sterling, A. C., Hudson, H. S., & Lemen, J. R. 2001, ApJ, **552**, 833

Priest, E. R., & Démoulin, P. 1995, J. Geophys. Res., 100, 23443

Titov, V. S., & Démoulin, P. 1999, A&A, **351**, 707

Titov, V. S., Hornig, G., & Démoulin, P. 2002, J. Geophys. Res., **107**, 1164

Titov, V. S. 2007, ApJ, **660**, 863

Titov, V. S., Downs, C., Mikić, Z., et al. 2018, ApJL, **852**, L21

Xia, C., Keppens, R., & Guo, Y. 2014, ApJ, **780**, 130